ACS Catalysis

Research Article

pubs.acs.org/acscatalysis

Correlating Ethylene Glycol Reforming Activity with In Situ EXAFS Detection of Ni Segregation in Supported NiPt Bimetallic Catalysts

Sarah A. Tupy,[†] Ayman M. Karim,[‡] Christina Bagia,[†] Weihua Deng,[†] Yulin Huang,[†] Dionisios G. Vlachos,*[,†] and Jingguang G. Chen*[,†]

[†]Catalysis Center for Energy Innovation, Department of Chemical and Bimolecular Engineering, University of Delaware, Newark, Delaware 19716, United States

[‡]Institute for Integrated Catalysis, Pacific Northwest National Laboratory, 902 Battelle Boulevard, Richland, Washington 99352, United States

Supporting Information

ABSTRACT: The structural changes in supported NiPt/C and NiPt/γ-Al_2O_3 catalysts were investigated using in situ extended X-ray absorption fine structure (EXAFS) under aqueous phase reforming (APR) of ethylene glycol conditions. Reverse Monte Carlo is introduced to analyze the EXAFS data. Parallel reactor studies of APR of ethylene glycol showed that NiPt catalysts were initially more active than monometallic Pt catalysts. The enhanced activity was correlated to changes in the catalyst structure. Under APR conditions, Ni segregated to the surface of the catalysts, resembling Ni-terminated bimetallic surfaces that were predicted to be more active than Pt from theoretical and experimental studies on model surfaces.

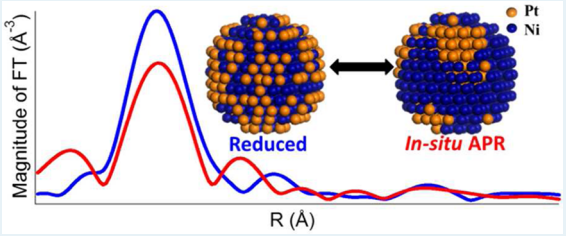

KEYWORDS: *In situ EXAFS, NiPt, ethylene glycol, supported catalysts, aqueous phase reforming, reverse Monte Carlo*

1. INTRODUCTION

Catalytic reforming may play a pivotal role in the utilization of biomass to produce hydrogen, which can be used locally in fuel cells, for hydrocarbon production (via Fischer−Tropsch) for transportation fuels,[1,2] and for on-site upgrading of bio-oils.[3] Aqueous phase reforming (APR) is a promising technology, especially for larger biomass derivatives, because of the following advantages: a single low temperature reactor is used, vaporization of biomass is not required, and low levels of CO are produced as a result of the aqueous environment.[4] APR reactor studies of biomass derivatives have been performed by several groups for a wide range of monometallic and bimetallic catalysts on different supports.[4−15] Focusing on the well-studied NiPt bimetallic system, the advantages of using bimetallic catalysts over monometallic catalysts have been demonstrated for the reforming of oxygenated molecules.

Ethylene glycol ($C_2H_6O_2$) has been often chosen as a model surrogate for studies for larger polyols.[4,7−9,13,16−21] The reforming pathways for ethylene glycol have been previously determined on single crystal surfaces using ultrahigh vacuum (UHV) techniques and density functional theory (DFT) calculations on both monometallic and bimetallic surfaces.[17,18,22−24] DFT calculations showed that the early dehydrogenation reaction steps should be kinetically important on Pt(111).[23] To verify the predicted reaction pathways, spectroscopic studies and temperature-programmed desorption (TPD) studies were employed.[22] For the NiPt(111) bimetallic surfaces, the activity trends for the reforming of ethylene glycol were experimentally found to be Pt−Ni−Pt < Pt < Ni < Ni−Pt−Pt.[22] For clarification of notation, Pt−Ni−Pt and Ni−Pt−Pt represent one monolayer of Ni occupying the subsurface and surface sites of Pt(111), respectively. Experimental results, which showed the surface Ni−Pt−Pt configuration to have the highest reforming activity for ethylene glycol, were consistent with microkinetic models that predicted the Ni-terminated bimetallic surface to be more active than a Pt monometallic surface.[25] On the basis of these studies, it is predicted that a Ni-terminated surface structure would be desirable for reforming of ethylene glycol over supported NiPt bimetallic catalysts.

To extend the model surfaces to supported NiPt catalysts, one important question is the relative thermodynamic stability of Ni-terminated and Pt-terminated bimetallic configurations under different reaction environments. UHV and DFT studies have been performed to study the stability and segregation of Ni in the NiPt bimetallic system.[26] Through computational and experimental techniques, the subsurface configuration of Pt−Ni−Pt has been shown to be thermodynamically more stable under vacuum and hydrogen atmosphere.[27,28] In addition, on supported bimetallic NiPt catalysts through a vibrational study of the characteristic frequencies of adsorbed CO, a Pt-terminated surface was confirmed.[29] Therefore, the desired Ni-terminated surface configuration predicted from model catalysts for reforming reactions is not stable after reduction in

Special Issue: Operando and In Situ Studies of Catalysis

Received: June 30, 2012
Revised: September 10, 2012
Published: September 17, 2012

   dx.doi.org/10.1021/cs3004227 | ACS Catal. 2012, 2, 2290−2296

H_2. However, in the presence of a strong absorbate, such as oxygen, it has been shown that the thermodynamic potential can be overcome, and Ni can segregate to the surface, favoring the surface configuration of Ni−Pt−Pt,[27] which was confirmed experimentally for both single crystal and polycrystalline NiPt bimetallic surfaces.[30] By switching reaction environments (reduction or oxidation), reversibility between Pt- and Ni-terminated surfaces of supported NiPt nanoparticle catalyst structure was reported by Mu et al.[31,32] Since the catalyst structure can change under reaction environments, in situ characterization of the supported catalyst under APR conditions is necessary to draw connections between the catalyst structure and activity.

Extended X-ray absorption fine structure (EXAFS) can be used to effectively obtain structural information.[33,34] Advances in techniques and opportunities to study catalysts under in situ conditions have been beneficial to gaining insight into the active sites under reaction conditions.[12,29,32,35,36] By performing in situ EXAFS under reducing and APR conditions, any structural changes, in particular the transformation from the undesirable Pt-terminated to the active Ni-terminated surface configuration can be determined. By performing steady-state activity experiments of APR of ethylene glycol in parallel, observed activity trends can be correlated with the structural changes of the supported catalyst obtained from in situ EXAFS data.

The primary objective of the current paper is to use in situ EXAFS to study the Ni segregation in supported NiPt bimetallic catalysts under APR environment, as compared with the reduced environment, to extend our understanding of the NiPt system. In addition, APR activity experiments on monometallic Pt and bimetallic NiPt were performed, and an enhanced activity was observed for the NiPt catalysts. In situ EXAFS studies showed a structural change in the NiPt catalyst switching from Pt-terminated after reduction to Ni-terminated during APR experiments. To aid in the understanding of the structural changes, structural nanoparticle modeling (reverse Monte Carlo (RMC)) was performed to correlate the coordination numbers from EXAFS with the extent of Pt and Ni termination in NiPt bimetallic particles. The combined in situ EXAFS, modeling of particles structures, and APR reactor studies indicate that Ni-terminated configuration is responsible for the enhanced APR activity of ethylene glycol. These results demonstrate the potential for using well-characterized model systems to identify active catalyst structures for oxygenate reforming.

2. EXPERIMENTAL METHODS

2.1. Catalyst Preparation and Characterization by CO Chemisorption. All catalysts (monometallic Pt and bimetallic NiPt with an atomic ratio 3:1 Ni/Pt) were prepared using a wet impregnation method. Tetraamineplatinum(II) nitrate (99.99% metals basis, Alfar Aesar) and nickel(II) nitrate hexahydate (99.99% metals basis, Alfar Aesar) were the precursors for Pt and Ni, respectively. Two materials, γ-Al_2O_3 (3 μm APS powder, Alfar Aesar) and activated carbon (TA-60, Picatal), were used as catalyst support. In a typical catalyst preparation procedure, metal precursor(s) was weighed to such that the final metal loading of Pt and Ni is 1.7 and 1.5 wt %, respectively. Additional details of catalyst preparation are given in the Supporting Information.

Chemisorption was performed to determine the CO uptake by using an AMI-200ip (Altamira Instruments). As previously described,[29] ~0.1 g of each catalyst was loaded into a quartz U tube and reduced under a mixture of 50% H_2/He at 450 °C for 1 h with a ramp rate of 14 °C/min. CO chemisorption was performed at 30 °C with a CO flow of 25 cm^3/min, followed by a pulse calibration carried out at 30 °C with the same CO flow. For both CO chemisorption and pulse calibration, a thermal conductivity detector (TCD) was used. The results are summarized in Table 1.

Table 1. Support Surface Area and CO Uptake on γ-Al_2O_3- and C-Supported Pt and NiPt Catalysts

active sites	support	support BET surface area (m^2/g) (from manufacturer)	chemisorption (μmol of CO/g)
Pt (1.7 wt %)	γ-Al_2O_3	80−120	43.1
Pt (1.7 wt %), Ni (1.5 wt %)	γ-Al_2O_3	80−120	47.7
Pt (1.7 wt %)	C	1100	51.2
Pt (1.7 wt %), Ni (1.5 wt %)	C	1100	53.2

2.2. Transmission Election Microscopy. Transmission electron microscopy (TEM) images were taken on "spent" NiPt/C catalyst after the APR experiments. Measurements were taken on a JEOL 2010F equipped with a Schottky field emission gun operated at 200 keV. Samples were prepared by suspending the catalysts in ethanol. A few drops of solution were pipetted onto a carbon-coated copper grid and allowed to dry. Images and particle distribution for the "spent" NiPt/C catalyst are shown in Figure 1. The average catalyst particle size is estimated to be 2.5 nm.

2.3. APR Reactor Experiments. All steady-state measurements were performed under the same reaction conditions (temperature of the reactor, pressure of the system, flow and concentration of the feed) using a high-pressure continuous

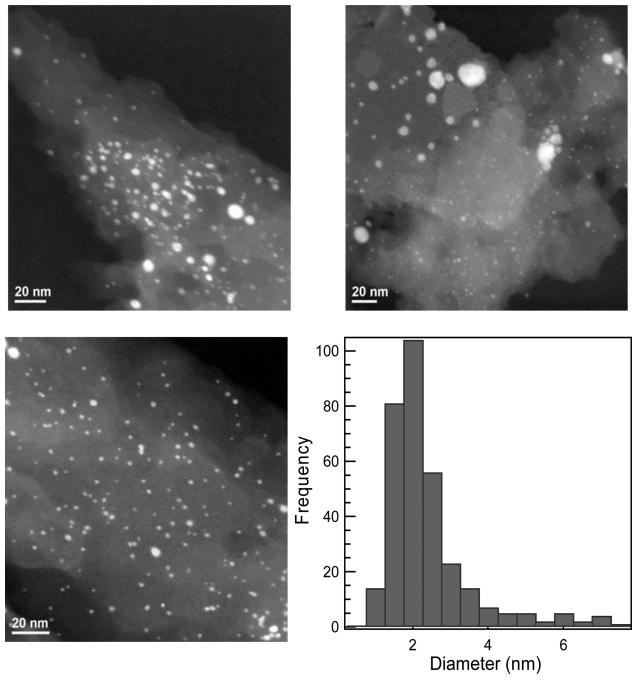

Figure 1. Representative STEM images of spent NiPt/C APR catalyst from reactor studies and particle size distribution. In total, 328 particles were measured using ImageJ software from 6 areas on 5 images. The average diameter of the catalyst particles was 2.5 nm.

dx.doi.org/10.1021/cs3004227 | ACS Catal. 2012, 2, 2290−2296

(up-)flow reactor. The reactor, a stainless steel tube with 1/4 in. o.d. and 19.5 in. length, was enclosed in a split tube furnace (Lindberg Blue M). A 300 mg portion of catalyst (sieved between 40 and 60 mesh (106−150 μm)) was packed into the middle of the reactor. Plugs of glass wool and quartz chips were used to secure the catalyst bed in place. Brooks mass flow controllers (model SLA5850) were used for delivering gases (H_2 and He). Each catalyst was reduced at 450 °C for 2 h in a 50% H_2/He mixture (total flow 100 cm^3/min). After reduction, the reactor was cooled to 25 °C, and pure He was used to flush the reactor. The system was pressurized with He up to 460 psig. A 10 v/v % ethylene glycol solution (prepared with deionized water) was pumped at a flow rate of 0.05 mL/min with an HPLC pump (ChromTech P2010 HPLC pump). The reactor was heated to the reaction temperature (230 °C) within 1 h. The total pressure of the system was maintained using a back pressure regulator (Swagelok). As a carrier gas, He (50 cm^3/min) was used to sweep the vapor reactor effluent to a gas chromatograph (GC). The gas-phase data were collected every hour to ensure that steady state was reached. The liquid samples were collected once, after 24 h of reaction.

2.4. Extended X-ray Absorption Fine Structure (EXAFS) Measurements. EXAFS measurements of the Pt L_3-edge and Ni K-edge were collected in H_2 and under APR conditions (see the Supporting Information for details) to determine the catalyst structure and whether it changes under reaction conditions. The experiments were performed on the X18B beamline at the National Synchrotron Light Source (NSLS), operated by the Synchrotron Catalysis Consortium (SCC) at Brookhaven National Laboratory.

The catalysts were characterized using an in-house-built in situ EXAFS cell, capable of probing working catalysts under APR conditions up to 1100 psig and 400 °C. The flow reactor consisted of either a 1.37 mm o.d. (1.0 mm i.d.) quartz or 3.1 mm o.d. (1.45 mm i.d.) glassy carbon tube (Tokai Carbon) in which the catalyst bed was kept in place using quartz wool on both sides. The tubes were connected to the rest of the system via standard Swagelok fittings using graphite ferrules (450 °C temperature rating). The experimental conditions during the EXAFS measurements can be found in the Supporting Information. Further details on the cell design are given elsewhere.[37]

The EXAFS data were collected in transmission mode with ionization chambers used as detectors. At the Pt L_3-edge, the measured absorption from the reactor tube walls was ∼67% for the quartz tube and ∼37% for the glassy carbon tube. At the Ni K-edge, the value was ∼80% and ∼67% from the tube walls for the quartz and glassy carbon tube, respectively. EXAFS data processing and analysis were performed using the Athena and Artemis programs of the IFEFFIT data analysis package.[38,39] Five scans were collected under each condition and merged after alignment using Pt (or Ni) foil reference spectrum collected simultaneously for each scan. $\chi(k)$ (where k is the photoelectron wavenumber) was obtained by subtracting smooth atomic background from the normalized absorption coefficient using the AUTOBK code. The theoretical EXAFS signal was constructed using the FEFF6 code[40] and fitted to the data in r-space using the Artemis program of the IFEFFIT package. The spectra were fitted in r-space by varying the coordination number of the single scattering path, CN; the bond length disorder (Debye−Waller factor), σ^2; the effective scattering length, R; and the correction to the threshold energy, ΔE_0. S_0^2 (the passive electron reduction factor) was obtained by first analyzing the Pt and Ni foils, and the best-fit values, 0.86 for Pt and 0.82 for Ni, were fixed during the fitting of the NiPt catalyst samples. The k-range used for Fourier transform of the $\chi(k)$ was 2.5−11 and 2.5−12 $Å^{-1}$, and the r-range for fitting was 1.7−3.0 and 1.2−2.8 Å for Pt L_3 and Ni K-edge, respectively.

2.5. Particle Modeling. Structural modeling of NiPt nanoparticles was used as a visualization tool for providing structural insight into the EXAFS data and to estimate the surface composition of the NiPt particles. Reverse Monte Carlo is a technique to reconstruct a structure based on experimental data and has previously been used to describe crystalline and amorphous systems.[41,42] Here, the RMC algorithm was employed to determine the spatial arrangement of Pt and Ni atoms within a particle structure to be consistent with parameters (coordination numbers) obtained from the EXAFS fits. A description of the modeling approach is given in the Supporting Information. This section will discuss assumptions used with the results and insights gained from structural modeling presented with the EXAFS discussion.

To model a nanoparticle, a spherical particle with a 2.5 nm diameter containing 555 atoms using the Pt fcc lattice was assumed (based on average particle size in Figure 1). Only parameters from the Pt L_3-edge were represented in the objective function and constraints (see Supporting Information). The exclusion of the Ni K-edge was due to hypothesized monometallic Ni particles in the experimental system, resulting from the 3:1 Ni/Pt atomic ratio used in the synthesis. This assumption was based on the fitting results of the EXAFS Ni K-edge spectra (see below), which showed large Ni−Ni and low Ni−Pt coordination numbers, suggesting the coexistence of large Ni rich particles and small bimetallic NiPt particles. The atomic composition of the particles in the particle modeling was set to a Ni/Pt atomic ratio of 3:1. Additional simulation results for different compositions and different cluster sizes are provided in the Supporting Information.

3. RESULTS AND DISCUSSION

3.1. Reactor Studies. APR of ethylene glycol was used as a probe reaction to study the activity of supported catalysts. The bimetallic NiPt catalysts show higher activity than the monometallic Pt catalysts. The activity trend is in agreement with previous work by Dumesic and co-workers.[7,8] Table 2 summarizes the conversion based on carbon dioxide, sum of gaseous products, and sum of all products (both gaseous and liquid phase) at 230 °C after 24 h reaction on the Pt and NiPt catalysts. The overall conversions for all the catalysts are relatively low (<20%). The enhanced activity in the NiPt catalysts over the Pt catalysts is evidenced by both an increase

Table 2. Carbon Conversion and Carbon Balances after 24 h of Reaction[a]

	Pt/γ-Al_2O_3	NiPt/γ-Al_2O_3	Pt/C	NiPt/C
	Conversion (%)			
CO_2	7.0	11.3	7.7	12.4
gas phase	7.8	12.0	8.7	13.3
total products	10.5	16.0	11.4	17.9
	Mass Balance (%)			
	97.3	100.6	98.2	100.3

[a]230 °C, 460 psig, 0.05 mL/min of 10 v/v% ethylene glycol feed solution.

dx.doi.org/10.1021/cs3004227 | ACS Catal. 2012, 2, 2290−2296

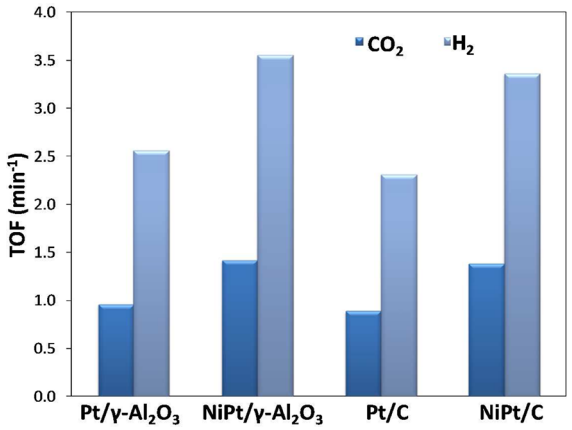

Figure 2. Hydrogen and carbon dioxide turnover frequencies for 10 v/v % ethylene glycol reforming on Pt/γ-Al_2O_3, NiPt/γ-Al_2O_3, Pt/C, and NiPt/C after 24 h of reaction.

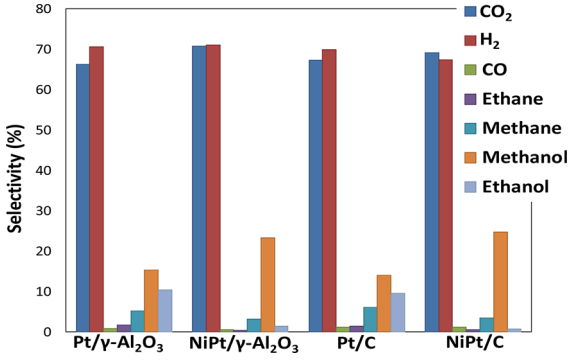

Figure 3. Carbon-based selectivity of products for all catalysts tested under APR conditions. Hydrogen selectivity is also provided.

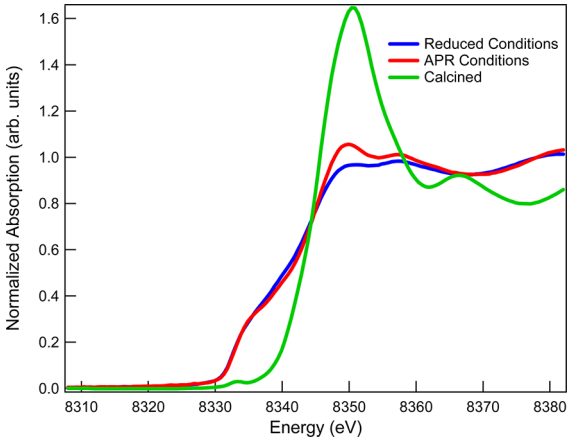

Figure 4. Normalized absorption spectra at the Ni K-edge for the NiPt/C before reduction (calcined), under 10% H_2 at 225 °C, and under APR reaction conditions (10 v/v % ethylene glycol in H_2O at 225 °C and 450 psig). The increase in white line intensity clearly shows partial oxidation of Ni under ethylene glycol APR reaction conditions.

(of nearly ~50%) in overall conversion and 40% higher rates (based on CO chemisorption) of H_2 produced, after 24 h of reaction. The turnover frequencies (TOF) for both hydrogen and carbon dioxide based on the CO chemisorption uptake are shown in Figure 2.

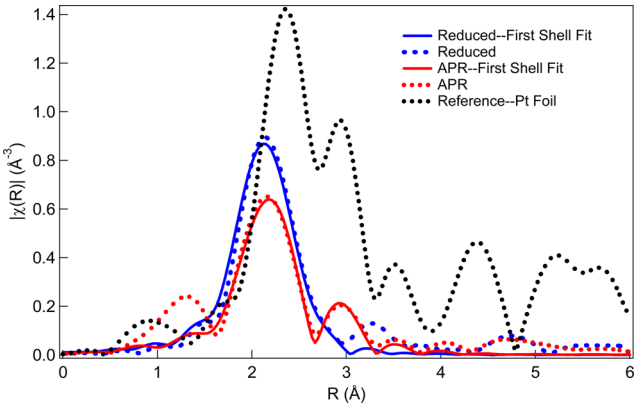

Figure 5. Magnitude of k^2-weighted Fourier transform of Pt L_3-edge EXAFS data, dashed lines, and fits, solid lines, for the NiPt/C catalyst under 10% H_2 at 225 °C (blue) and under APR reaction conditions (red, 10 v/v % ethylene glycol in H_2O at 225 °C and 450 psig). For reference, the Pt foil is in black. The catalyst was reduced at 350 °C in 10% H_2 for 2 h prior to the EXAFS data scans.

APR of 10 v/v % ethylene glycol solution produced primarily carbon dioxide and hydrogen; however, small amounts of gaseous alkanes (ethane, methane), carbon monoxide, and organic liquid phase (methanol, ethanol) byproducts were also detected (Figure 3). Additional details on long time on stream activity are provided in the Supporting Information.

3.2. EXAFS Measurements and Particle Modeling. To understand the cause of the enhanced activity, the structural transformation of the supported NiPt bimetallic catalysts was studied under APR conditions. In this section, in situ EXAFS results of NiPt/C are presented and discussed to highlight the structural transformation under APR conditions. Similar results are obtained for NiPt/γ-Al_2O_3, which are provided in the Supporting Information. The Ni K-edge XANES spectra for the calcined, reduced catalyst under H_2 and under APR are shown in Figure 4. It can be seen that, under APR reaction conditions, Ni gets partially oxidized. The Ni K-edge EXAFS fitting results in Table 3 show that Ni gets fully reduced and that the APR reaction conditions result in partial oxidation. The large Ni−Ni and low Ni−Pt coordination numbers suggest that large Ni rich particles coexist with the small NiPt alloy nanoparticles. Therefore, the structural information of the NiPt nanoparticles can only be extracted from the Pt L_3-edge.

Figure 5 shows the magnitude of k^2-weighted EXAFS Pt L_3-edge spectra for NiPt/C under 10% H_2 and under ethylene glycol APR conditions. It is useful to qualitatively compare the spectra before describing the fitting results. Both spectra differ significantly from that of a monometallic Pt, suggesting the formation of NiPt alloy. The spectrum under 10% H_2 shows a higher peak intensity at ~2.1 Å compared with the spectrum under APR. It can also be seen that the peak is shifted to lower distance compared with that under APR. In addition, the spectrum under APR shows an additional peak at ~2.9 Å, which is most likely due to an increase in Pt−Pt coordination. The qualitative evaluation of the spectra in Figure 5 suggests a higher contribution from Pt−Ni scattering path (~2.1 Å in r-space) and a lower contribution from Pt−Pt scattering path under H_2 compared with the spectrum under APR. In other words, the coordination number for Pt−Pt appears to increase while that of Pt−Ni appears to decrease under APR compared with the reduced catalyst. The fitting results of the Pt L_3-edge spectra are shown in Table 4.

dx.doi.org/10.1021/cs3004227 | ACS Catal. 2012, 2, 2290−2296

Table 3. Fitting Results for the NiPt/C Catalyst at the Ni K-Edge

Condition	10% H_2 at 50 °C[a]	10% H_2 at 225 °C[a]	APR at 225 °C[b]	After APR 10% H_2 at 50 °C[c]
CN(Ni−Ni)	8.2 ± 0.5	8.0 ± 0.2	8.7 ± 0.4	8.3 ± 0.4
CN(Ni−Pt)	0.4 ± 0.4	0.0 ± 0.2	0.5 ± 0.7	0.5 ± 0.3
CN(Ni−O)			0.83 ± 0.02	
R(Ni−Ni), Å	2.488 ± 0.003	2.480 ± 0.002	2.483 ± 0.003	2.490 ± 0.003
R(Ni−Pt), Å	2.552 ± 0.008	2.535 ± 0.006	2.64 ± 0.03	2.567 ± 0.007
R(Ni−O), Å			2.03 ± 0.02	
σ^2(Ni−Ni), Å^2	0.0079 ± 0.0004	0.0106 ± 0.0002	0.0091 ± 0.0009	0.0075 ± 0.0003
σ^2(Ni−Pt), Å^2	0.007 ± 0.001	0.010 ± 0.004	0.011 ± 0.003	0.006 ± 0.001
ΔE_0, eV	5.6 ± 0.3	4.8 ± 0.4	5.8 ± 0.6	5.8 ± 0.4

[a]The catalyst was reduced in 10% H_2/He at 350 °C for 2 h before exposure to the APR reaction conditions. [b]APR conditions: 10 v/v% ethylene glycol in H_2O at 225 °C and 450 psig. [c]The catalyst was reduced in 10% H_2/He at 350 °C for 1 h after exposure to the APR reaction conditions.

Table 4. Fitting Results for the NiPt/C Catalyst at the Pt L_3-Edge[a]

Condition	10% H_2 at 50 °C[1]	10% H_2 at 225 °C[1]	APR at 225 °C[2]	After APR 10% H_2 at 50 °C[3]
CN(Pt-Pt) Experimental	1.9 ± 0.8	2.0 ± 0.7	6.0 ± 1.4	2.8 ± 0.9
CN(Pt-Ni) Experimental	3.5 ± 0.4	3.8 ± 0.3	1.9 ± 0.8	4.6 ± 0.4
CN(Pt-Pt) Simulation	2.41 ± 0.01	2.47 ± 0.02	6.2 ± 0.1	3.31 ± 0.03
CN(Pt-Ni) Simulation	4.230 ± 0.009	4.39 ± 0.01	3.46 ± 0.02	5.42 ± 0.02
R(Pt-Pt), Å	2.65 ± 0.03	2.64 ± 0.03	2.67 ± 0.02	2.69 ± 0.03
R(Pt-Ni), Å	2.548 ± 0.007	2.530 ± 0.008	2.64 ± 0.03	2.566 ± 0.008
σ^2(Pt-Pt), Å^2	0.008 ± 0.003	0.011 ± 0.002	0.010 ± 0.002	0.007 ± 0.002
σ^2(Pt-Ni), Å^2	0.007 ± 0.001	0.010 ± 0.004	0.011 ± 0.003	0.006 ± 0.001
ΔE_0 (eV)	2.5 ± 1.0	2.5 ± 0.6	4.0 ± 0.8	8.0 ± 0.9

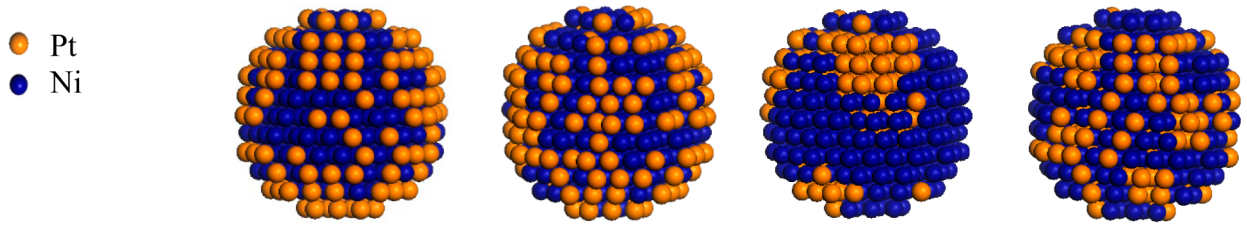

[a]Simulation results are also included. The catalyst was reduced in 10% H_2/He at 350 °C for 2 h before[1] and 1 h after[3] exposure to the APR reaction conditions. [2]APR conditions: 10 v/v% ethylene glycol in H_2O at 225 °C and 450 psig. Simulation error bars reported are 95% confidence interval from 30 simulations for a spherical particle with fixed diameter (2.5 nm) and composition (25% Pt, 75% Ni). Percentage of atoms at the surface (outer most layer), subsurface (second layer), and core (rest of nanoparticle) locations are 34, 30, and 36%, respectively.

The detection of Pt−Ni coordination clearly shows the formation of NiPt alloy after the reduction of the catalyst. For the reduced catalyst, a small Pt−Pt coordination number and a relatively larger Pt−Ni coordination number coupled with a short Pt−Ni bond (2.53 Å) all suggest that the NiPt nanoparticles form a core−shell structure in which the core is rich in Ni and the shell is rich in Pt. The Pt-rich shell/Ni-rich core structure is not preserved under APR, and the NiPt nanoparticles undergo restructuring, confirming the qualitative observations from Figure 5, and can be visually observed from simulation results given in Table 4. Specifically, the Pt−Pt coordination number increases significantly (from 2.0 to 6.0), while the Pt−Ni coordination number decreases (from 3.8 to 1.9). This is also accompanied by a large increase in the Pt−Ni bond length from 2.53 Å for the reduced catalyst to 2.64 Å. These results suggest that under APR, Pt atoms diffuse to the core of the nanoparticles while Ni segregates to the surface. Remarkably, rereduction of the catalyst results in restructuring of the NiPt nanoparticles back to the Pt-rich shell/Ni-rich core. This can be seen in a decrease in the Pt−Pt coordination number, an increase in the Pt−Ni coordination number, and a decrease in the Pt−Ni bond length to values similar to that of the reduced catalyst prior to exposure to APR. These results also indicate that the changes observed under reaction conditions are not a result of segregation of Pt and Ni into separate particles. It should be noted that the increase in the total Pt coordination number (Pt−Pt + Pt−Ni) under APR reaction conditions and also for the rereduced catalyst suggests that APR reaction conditions resulted in sintering of the NiPt nanoparticles.

To enhance the understanding of restructuring related to coordination numbers, structural modeling was employed. Examples of optimized nanoparticle configurations and results are given in Table 4. On the basis of the constraints defined (see Supporting Information), the simulated results are consistent with the experimentally measured coordination numbers. The trends for changes in CN_{Pt-Pt} and CN_{Pt-Ni} when exposed to different reaction conditions are in qualitative agreement among experiment and simulation. As discussed above, ΔCN_{Pt-Ni} decreases while ΔCN_{Pt-Pt} increases when

dx.doi.org/10.1021/cs3004227 | ACS Catal. 2012, 2, 2290−2296

transitioning from reduced conditions to APR conditions. In agreement with the interpretation of this observation from experimental data, simulation results visually show that Ni segregates to the surface of the nanoparticle under APR conditions. The locations of Pt and Ni atoms in a particle are determined. Table 5 gives the percentage of each location that is composed of Pt. The percentages of total Pt at each location is given in the Supporting Information. Under reduced conditions, the majority of the surface is covered with Pt, which is consistent with previous idealized studies,[27−29,31] whereas under APR conditions, the surface is ∼70% covered by Ni.

Table 5. Results from Modeling of NiPt/C Catalyst[a]

	% of surface that is Pt	% of subsurface that is Pt	% of core that is Pt
10% H_2 at 50 °C	73.5 ± 0.1	0.8 ± 0.2	0 ± 0
10% H_2 at 225 °C	69.2 ± 0.3	5.5 ± 0.4	0.0 ± 0.1
APR at 225 °C	30 ± 1	25 ± 1	20 ± 2
After APR 10% H_2 at 50 °C	42.7 ± 0.4	21 ± 1	11.9 ± 0.8

[a]Average percentages of locations composed of Pt. Simulation error bars reported are the 95% confidence interval from 30 simulations for a spherical particle with fixed diameter (2.5 nm) and composition (25% Pt, 75% Ni). Percentage of atoms at the surface (outermost layer), subsurface (second layer), and core (rest of nanoparticle) locations are 34, 30, and 36%, respectively.

From the particle modeling results, it can be seen that the TOF values for NiPt-supported catalysts reported in Figure 2 are underestimated, since under APR conditions, the surface of the nanoparticles is mostly covered by Ni. Consequently, for NiPt, the TOF normalized to the Pt surface sites under APR conditions is expected to be much higher than what is reported in Figure 2. Although using XANES of chemisorbed CO has been used to estimate the percent of exposed Pt for bimetallic catalysts,[12] it would not work for bimetallic systems in which restructuring occurs under reaction conditions. For bimetallic catalysts, the methodology of combining in situ EXAFS with structural modeling, as reported in this work, is a useful tool in estimating the surface composition of small nanoparticles.

CONCLUSIONS

APR of ethylene glycol over supported NiPt and Pt catalysts showed that, after 24 h on stream, the NiPt catalyst is more active than Pt. In situ EXAFS studies verified that the surface of the NiPt catalysts is mainly Pt-terminated in a H_2 environment. Under in situ APR conditions, Ni segregation occurs to produce a Ni-enriched surface, as determined from EXAFS and by using reverse Monte Carlo simulation. The enhanced activity observed for the NiPt bimetallic catalyst in the APR studies is likely due to the Ni-terminated surface, which is consistent with the predictions from previous DFT and UHV studies. In situ experiments also show that upon rereduction of the "spent" catalyst, the Ni segregation can be reversed, resulting in a Pt-enriched surface. This reversibility highlights advantages and disadvantages of bimetallic catalysts. The ability for the catalyst to restructure shows the range and versatility of a catalyst to be used for various chemistries. However, the facile movement of metal atoms under APR conditions points out challenges in understanding and maintaining the long-term stability of bimetallic catalysts for APR.

ASSOCIATED CONTENT

Supporting Information

Details about catalyst preparation, analytical techniques, definitions used, long-term catalyst activity, reaction conditions during EXAFS, additional EXAFS figures on Ni K-edge and Pt L_3-edge for NiPt/C, EXAFS figure and fitting results for NiPt/γ-Al_2O_3, particle modeling, and estimates of surface composition of nanoparticles. This material is available free of charge via the Internet at http://pubs.acs.org.

AUTHOR INFORMATION

Corresponding Author

*E-mails: (J.G.C.) jgchen@udel.edu, (D.G.V.) vlachos@udel.edu.

Notes

The authors declare no competing financial interest.

ACKNOWLEDGMENTS

The University of Delaware authors acknowledge support from the Catalysis Center for Energy Innovation, an Energy Frontier Research Center funded by the U.S. Department of Energy, Office of Science, Office of Basic Energy Sciences under Award No. DE-SC0001004. The Pacific Northwest National Laboratory author acknowledges support from the U.S. Department of Energy, Office of Energy Efficiency and Renewable Energy and from the National Advanced Biofuels Consortium, which is funded by the Department of Energy's Office of Biomass Program with recovery act funds. Use of the National Synchrotron Light Source, Brookhaven National Laboratory, for the EXAFS experiments was supported by the US Department of Energy, Office of Basic Energy Sciences (Grant No. DE-FG02-05ER15688). S.A.T. is grateful to Prof. George W. Huber and Dr. Tushar Vispute for APR training and Vassili S. Vorotnikov for useful discussions.

REFERENCES

(1) Skoplyak, O.; Barteau, M. A.; Chen, J. G. *ChemSusChem* **2008**, *1*, 524−526.
(2) Soares, R. R.; Simonetti, D. A.; Dumesic, J. A. *Angew. Chem., Int. Ed.* **2006**, *45*, 3982−3985.
(3) Elliott, D. C. *Energy Fuels* **2007**, *21*, 1792−1815.
(4) Davda, R. R.; Shabaker, J. W.; Huber, G. W.; Cortright, R. D.; Dumesic, J. A. *Appl. Catal., B* **2005**, *56*, 171−186.
(5) He, R.; Davda, R. R.; Dumesic, J. A. *J. Phys. Chem. B* **2005**, *109*, 2810−2820.
(6) Huber, G. W.; Dumesic, J. A. *Catal. Today* **2006**, *111*, 119−132.
(7) Huber, G. W.; Shabaker, J. W.; Evans, S. T.; Dumesic, J. A. *Appl. Catal., B* **2006**, *62*, 226−235.
(8) Shabaker, J. W.; Huber, G. W.; Davda, R. R.; Cortright, R. D.; Dumesic, J. A. *Catal. Lett.* **2003**, *88*, 1−8.
(9) Shabaker, J. W.; Davda, R. R.; Huber, G. W.; Cortright, R. D.; Dumesic, J. A. *J. Catal.* **2003**, *215*, 344−352.
(10) King, D. L.; Zhang, L. A.; Xia, G.; Karim, A. M.; Heldebrant, D. J.; Wang, X. Q.; Peterson, T.; Wang, Y. *Appl. Catal., B* **2010**, *99*, 206−213.
(11) Ciftci, A.; Peng, B.; Jentys, A.; Lercher, J. A.; Hensen, E. J. M. *Appl. Catal., A* **2012**, *431−432*, 113−119.
(12) Dietrich, P.; Lobo-Lapidus, R.; Wu, T.; Sumer, A.; Akatay, M.; Fingland, B.; Guo, N.; Dumesic, J.; Marshall, C.; Stach, E.; Jellinek, J.; Delgass, W.; Ribeiro, F.; Miller, J. *Top. Catal.* **2012**, *55*, 53−69.
(13) Liu, J.; Sun, B.; Hu, J. Y.; Pei, Y.; Li, H. X.; Qiao, M. H. *J. Catal.* **2010**, *274*, 287−295.
(14) Zhang, L.; Karim, A. M.; Engelhard, M. H.; Wei, Z. H.; King, D. L.; Wang, Y. *J. Catal.* **2012**, *287*, 37−43.

(15) Ravenelle, R. M.; Copeland, J. R.; Kim, W. G.; Crittenden, J. C.; Sievers, C. *ACS Catal.* **2011**, *1*, 552−561.
(16) Dauenhauer, P. J.; Salge, J. R.; Schmidt, L. D. *J. Catal.* **2006**, *244*, 238−247.
(17) Skoplyak, O.; Barteau, M. A.; Chen, J. G. G. *Surf. Sci.* **2008**, *602*, 3578−3587.
(18) Skoplyak, O.; Menning, C. A.; Barteau, M. A.; Chen, J. G. G. *Top. Catal.* **2008**, *51*, 49−59.
(19) Kandoi, S.; Greeley, J.; Simonetti, D.; Shabaker, J.; Dumesic, J. A.; Mavrikakis, M. *J. Phys. Chem. C* **2011**, *115*, 961−971.
(20) Ji, N.; Zhang, T.; Zheng, M. Y.; Wang, A. Q.; Wang, H.; Wang, X. D.; Chen, J. G. G. *Angew. Chem., Int. Ed.* **2008**, *47*, 8510−8513.
(21) Yue, H. R.; Zhao, Y. J.; Ma, X. B.; Gong, J. L. *Chem. Soc. Rev.* **2012**, *41*, 4218−4244.
(22) Skoplyak, O.; Barteau, M. A.; Chen, J. G. G. *J. Phys. Chem. B* **2006**, *110*, 1686−1694.
(23) Salciccioli, M.; Yu, W. T.; Barteau, M. A.; Chen, J. G. G.; Vlachos, D. G. *J. Am. Chem. Soc.* **2011**, *133*, 7996−8004.
(24) Christiansen, M. A.; Vlachos, D. G. *Appl. Catal., A* **2012**, *431*−*432*, 18−24.
(25) Salciccioli, M.; Vlachos, D. G. *ACS Catal.* **2011**, *1*, 1246−1256.
(26) Menning, C. A.; Chen, J. G. *Top. Catal.* **2010**, *53*, 338−347.
(27) Menning, C. A.; Chen, J. G. G., *J. Chem. Phys.* **2009**, *130*, DOI: 10.1063/1.3125926.
(28) Menning, C. A.; Hwu, H. H.; Chen, J. G. G. *J. Phys. Chem. B* **2006**, *110*, 15471−15477.
(29) Lonergan, W. W.; Vlachos, D. G.; Chen, J. G. G. *J. Catal.* **2010**, *271*, 239−250.
(30) Menning, C. A.; Chen, J. G. *J. Power Sources* **2010**, *195*, 3140−3144.
(31) Mu, R. T.; Fu, Q.; Liu, H. Y.; Tan, D. L.; Zhai, R. S.; Bao, X. H. *Appl. Surf. Sci.* **2009**, *255*, 7296−7301.
(32) Mu, R. T.; Guo, X. G.; Fu, Q.; Bao, X. H. *J. Phys. Chem. C* **2011**, *115*, 20590−20595.
(33) Sinfelt, J. H.; Via, G. H.; Meitzner, G.; Lytle, F. W. *ACS Symp. Ser.* **1985**, *288*, 253−266.
(34) Teo, B. K. *Basic Principles and Data Analysis*; Springer-Verlag: Berlin; New York, 1986.
(35) Frenkel, A. I.; Wang, Q.; Marinkovic, N.; Chen, J. G.; Barrio, L.; Si, R.; Lopez Camara, A.; Estrella, A. M.; Rodriguez, J. A.; Hanson, J. C. *J. Phys. Chem. C* **2011**, *115*, 17884−17890.
(36) Paredis, K.; Ono, L. K.; Mostafa, S.; Li, L.; Zhang, Z. F.; Yang, J. C.; Barrio, L.; Frenkel, A. I.; Cuenya, B. R. *J. Am. Chem. Soc.* **2011**, *133*, 6728−6735.
(37) Karim, A. M.; Howard, C.; Roberts, B.; Kovarik, L.; Zhang, L.; King, D.; Wang, Y. *ACS Catal.* **2012**, Accepted. DOI: 10.1021/cs3005049.
(38) Ravel, B.; Newville, M. *J. Synchrotron Radiat.* **2005**, *12*, 537−541.
(39) Newville, M. *J. Synchrotron Radiat.* **2001**, *8*, 96−100.
(40) Zabinsky, S. I.; Rehr, J. J.; Ankudinov, A.; Albers, R. C.; Eller, M. J. *Phys. Rev. B* **1995**, *52*, 2995−3009.
(41) Gurman, S. J.; McGreevy, R. L. *J. Phys.: Condens. Matter* **1990**, *2*, 9463−9473.
(42) McGreevy, R. L. *J. Phys.: Condens. Matter* **2001**, *13*, R877−R913.